

Melting Experiments on Fe-O-H and Fe-H: Evidence for Eutectic Melting in Fe-FeH and Implications for Hydrogen in the Core

Kenta Oka¹, Nagi Ikuta¹, Shoh Tagawa^{1,2}, Kei Hirose^{1,2}, and Yasuo Ohishi³

¹Department of Earth and Planetary Science, The University of Tokyo, Bunkyo, Tokyo, Japan

²Earth-Life Science Institute, Tokyo Institute of Technology, Meguro, Tokyo, Japan

³Japan Synchrotron Radiation Research Institute, SPring-8, Sayo, Hyogo, Japan

Key Points:

- We examined the liquidus phase relations and solid/liquid partitioning in the Fe-O±H and Fe-H systems at ~40 GPa and ~150 GPa.
- Eutectic melting between Fe and FeH is indicated from the phase relations and melting temperature in Fe-O-H and Fe-H.
- The outer core may include 2.9–5.2 wt% O, 0.03–0.32 wt% H, 0–3.4 wt% Si, and 1.7 wt% S.

Abstract We examined liquidus phase relations in Fe-O±H at ~40 and ~150 GPa, and in Fe-H at 45 GPa. While it has been speculated that Fe and FeH form continuous solid solution to core pressures, our experiment on Fe-H showed that FeH_{0.20} forms with the hcp structure, different from fcc for stoichiometric FeH, and melts at temperature lower than that for FeH, suggesting eutectic melting between Fe and FeH. It is consistent with the liquidus phase diagram in Fe-O-H, which implies the Fe-FeH binary eutectic liquid composition of FeH_{0.42} at ~40 GPa. We estimated the outer core liquid composition to be Fe + 2.9–5.2% O + 0.03–0.32% H + 0–3.4% Si + 1.7% S by weight, based on the liquidus phase relations, solid-liquid partitioning, and outer/inner core densities and velocities, indicating that O and either H or Si are important core light elements.

Plain Language Summary We have investigated the melting phase relations in the Fe-O±H and Fe-H systems at high pressures in a laser-heated diamond-anvil cell. The solid-liquid partition coefficient of H was also determined. While it is known that Fe and stoichiometric FeH form continuous solid solution at least to ~20 GPa, our experiments on the Fe-O-H ternary and Fe-H binary systems performed at ~40 GPa consistently suggested eutectic melting between Fe and FeH with eutectic liquid composition of FeH_{0.42}. We explored the possible range of the Earth's liquid core

35 composition, which should be 1) within the liquidus field of Fe to crystallize the dense
36 inner core, 2) compatible with seismological observations of the outer core, and 3) in
37 chemically equilibrium with the inner core solid that explains the observed density and
38 velocities. The results indicate that the outer core is rich in O and either H or Si,
39 supporting the delivery of a large amount of water to the Earth found in recent planet
40 formation theories and its sequestration into the metallic core that is also inferred from
41 metal-silicate partitioning data.

42 **1. Introduction**

43 The Earth's core should contain more than one light impurity elements (see recent
44 reviews by Li & Fei, 2014 and Hirose et al., 2021). Both O and H can be important core
45 light elements because the density and sound velocity observed in the outer core are
46 compatible with the presence of O (Badro et al., 2014) and H (Umemoto & Hirose,
47 2015, 2020). Recent planet formation models suggested that 10 to 100 times ocean mass
48 of water may have been brought to the Earth during its accretion (e.g., Raymond et al.,
49 2007; Walsh et al., 2011). The chemical reaction of solar-nebula-type H-rich
50 proto-atmosphere with a magma ocean could have been another source of water (Ikoma
51 & Genda, 2006; Olson & Sharp, 2019). It is likely that most of H₂O was once dissolved
52 into a magma ocean, and H and O were incorporated into core-forming metals during
53 their segregation from silicate (Tagawa et al., 2021; Li et al., 2020; Yuan & Steinle-
54 Neumann, 2020).

55 Liquidus phase relations of Fe alloy systems, in particular the liquidus field of Fe (a
56 compositional range of liquids that first crystallize Fe), constrain the outer core
57 composition (e.g., Yokoo et al., 2019; Hasegawa et al., 2021; Sakai & Hirose, 2021).
58 When O and H are two major core light elements, the liquid core should not crystallize
59 FeO nor FeH but Fe at the inner core boundary (ICB), otherwise the denser solid inner
60 core is not formed. In order to understand the liquidus phase relations in the Fe-O-H
61 system, the knowledge on the relevant binary systems is helpful. Previous high-pressure
62 experiments demonstrated that O concentration in the Fe-FeO eutectic liquid increases
63 with increasing pressure (Morard et al., 2017; Oka et al., 2019). The recent study by
64 Oka and others based on experiments to 204 GPa estimated 15 wt% O in the Fe-FeO
65 binary eutectic liquid at ICB. On the other hand, earlier high-pressure melting
66 experiments on the Fe(\pm Ni)-H system were limited to 20 GPa (Sakamaki et al., 2009;
67 Imai, 2013; Shibazaki et al., 2014) because of a technical difficulty in dealing with
68 hydrogen. Fukai (1992) speculated continuous solid solution between Fe and

69 stoichiometric FeH to megabar pressure, but it has been verified only to ~ 20 GPa (Imai,
70 2013; Shibazaki et al., 2014).

71 In this study, we have carried out melting experiments on the Fe-O \pm H and Fe-H systems
72 at ~ 40 GPa and ~ 150 GPa. Our results on Fe-O-H suggest that Fe-FeH is an eutectic
73 system, which contradicts the phase diagram supposed by Fukai (1992) but is supported
74 by our experiment on Fe-H alloy. Our findings of 1) eutectic melting between Fe and
75 FeH, 2) liquidus phase relations in the Fe-O-H system, and 3) the solid-liquid
76 partitioning of H help to constrain concentrations of O, H, and other light elements in
77 the outer core.

78 **2. Results**

79 We have examined the melting phase relations in the Fe-O \pm H and Fe-H systems on the
80 basis of high-pressure and -temperature (P - T) experiments using laser-heated
81 diamond-anvil cell (DAC) techniques, combined with in-situ synchrotron X-ray
82 diffraction (XRD) measurements and ex-situ textural and compositional
83 characterizations using electron microprobes (see Experimental Methods in the
84 Supporting Information).

85 **2.1. Melting in Fe-O \pm H**

86 A total of six separate melting experiments were carried out in the Fe-O \pm H system at
87 ~ 40 GPa and ~ 150 GPa (runs #A1–A6 in [Table S1](#)). For all runs, we performed
88 synchrotron XRD measurements and subsequent microprobe observations on recovered
89 samples. In run #A4, while the intense peaks from hcp Fe were present before heating,
90 they were almost lost and alternatively a diffuse signal characteristic of liquid was
91 observed around 12 degrees of two-theta angle upon heating to 2370 K ([Figure 1a](#)).
92 Upon quenching temperature, the peaks of fcc FeH $_x$ ($x = 0.31$) appeared from the liquid
93 portion. The XRD pattern obtained at ~ 12 μm away from the center of a laser-heated
94 spot included strong peaks from rhombohedrally-distorted B1 FeO and hcp FeH $_{0.24}$.

95 This sample was recovered from a DAC, and in its cross section, there was a chemically
96 homogeneous area with a non-stoichiometric composition at the center, which
97 represents a quenched liquid ([Figures 2a, b](#)). The earlier DAC experiments by Hirose et
98 al. (2019) and Tagawa et al. (2021) demonstrated that the H content in FeH $_x$ crystals
99 formed from liquid upon quenching temperature closely represents that of Fe-H liquid.
100 We therefore consider that Fe-O-H liquids in the present experiments were fully

101 quenched into a mixture of solid FeH_x and FeO . The proportion of FeO was obtained
102 from the EPMA analysis of O concentration in the quenched liquid. The remaining
103 phase proportion of FeH_x and its H concentration x that was estimated from its lattice
104 volume in XRD patterns give 0.49 wt% H in the Fe-O-H liquid (Table S1). Next to the
105 liquid pool, electron microprobe images showed a couple of single-phase layers of Fe
106 and FeO (Figures 2a, b). According to the XRD observations, the Fe layer had been
107 solid $\text{FeH}_{0.24}$ (Fe + 0.43 wt% H) before it lost hydrogen during decompression (Figure
108 1a). The partition coefficient of H between solid Fe and liquid, D_H (solid/liquid), was
109 0.89 on weight basis. The liquid was in direct contact with the FeO layer or in some
110 place with the $\text{FeH}_{0.24}$ layer, indicating that both FeO and $\text{FeH}_{0.24}$ are the liquidus phases
111 of the Fe-O-H liquid formed in run #A4. The outside of these liquidus phase layers was
112 not melted. Runs #A1–A3 were carried out around 40 GPa in a similar manner with
113 changing the Fe/ H_2O ratio in the starting materials (Table S1). These liquids included
114 0.1–0.4 wt% C except 1.7 wt% C in run #A1.

115 In runs #A5 and #A6 performed at ~150 GPa, liquids were crystallized into the hcp
116 phase upon quenching temperature to 300 K, which included minimal amounts of H
117 (<0.04 wt%) (Table S1). The EPMA data showed 10.4–13.0 wt% O and 0.9–3.7 wt% C
118 in quenched liquids, indicating they were Fe-O±C liquids. The liquid
119 Fe-13.0wt%O-0.9wt%C obtained in run #A5 coexisted with solid Fe, giving the lower
120 bound for O concentration in the Fe-FeO binary eutectic liquid at 147 GPa (Figure S1).
121 It helps to constrain the change in the eutectic liquid composition in the Fe-FeO system
122 with increasing pressure, which was previously estimated only with a single datum
123 point above 50 GPa in Oka et al. (2019).

124 2.2. Melting in Fe-H

125 Melting experiment was carried out also on the Fe-FeH binary system at 45 GPa (run
126 #B, Table S2) (see Experimental Methods in the Supporting Information).
127 Non-stoichiometric hcp $\text{FeH}_{0.30}$ was synthesized by heating to <1000 K at 10 GPa
128 (Figure 1b). The excess molecular H_2 in a sample chamber was lost to a neighboring
129 rhenium gasket to form Re-H alloy upon compression to 23 GPa at room temperature
130 (Scheler et al., 2011). After further compression, we melted this sample by heating to
131 1900 K for 80 sec at 45 GPa. The hcp 002, 101, and 102 peaks were observed in the
132 XRD pattern during heating, and the presence of liquid was confirmed when quenching
133 temperature by the appearance of the new hcp 100 and 110 peaks and of the hcp 002,
134 101 and 102 additional spot peaks in the 2D XRD image. We found the H content in

135 liquid to be $\text{FeH}_{0.26}$ from these hcp peaks that emerged upon temperature quench
136 (Figure 1b). The solid phase that coexisted with liquid was hcp $\text{FeH}_{0.20}$ based on spot
137 peaks that were present during heating. These results show the solid/liquid partition
138 coefficient of H, $D_{\text{H}} = 0.77$ on weight basis. Carbon contamination should have been
139 minor in this experiment because the sample was heated only to 1900 K, much less than
140 in other melting experiments on Fe-O-H.

141 3. Discussion

142 3.1. Eutectic Melting in Fe-FeH and the Liquidus Phase Relations in Fe-O-H

143 The high-pressure phase relations in the Fe-H system have been speculated by Fukai
144 (1992), suggesting 1) continuous solid solution between Fe and FeH and 2) an eutectic
145 composition with FeH_x ($x > 1$). The multi-anvil experiments by Imai (2013) and
146 Shibazaki et al. (2014) reported the melting and subsolidus phase relations in the
147 Fe-FeH(\pm Ni) system to 15–20 GPa, which are consistent with the phase diagram
148 supposed by Fukai (1992). In contrast, in the present experiment (run #B), melting
149 occurred by heating to 1900 K at 45 GPa, lower than the melting point of 2100 K for
150 stoichiometric FeH (Tagawa, Helffrich et al., 2022) (note that if Fe and FeH form
151 continuous solid solution, the solidus temperature of $\text{FeH}_{0.20-0.30}$ should be closer to the
152 melting point of pure Fe than that of FeH). In addition, we found $\text{FeH}_{0.20}$ with the hcp
153 structure at this P - T condition, which is different from the fcc structure for FeH (Kato et
154 al., 2020; Thompson et al., 2018; Tagawa, Gomi et al., 2022). It indicates a gap in solid
155 solution between Fe and FeH. These suggest eutectic (not peritectic) melting between
156 the H-poor hcp and H-rich fcc phases in the Fe-FeH system. The presence of the gap in
157 solid solution between hcp Fe and fcc FeH and the resulting eutectic melting are likely
158 to be hold to Earth's inner core conditions (Tagawa, Helffrich et al., 2022).

159 The compositions of liquids obtained at \sim 40 GPa in runs #A1–A4 and #B are plotted in
160 the Fe-O-H ternary diagram (Figure 3a). The liquid compositions found in runs #A2 and
161 #A3 should be within the liquidus field of FeO, and that in run #A4 is on the Fe + FeO
162 cotectic line (showing the liquid compositions coexisting with both Fe and FeO).
163 Considering the eutectic point in the Fe-FeO binary (Figure S1), the position of the Fe +
164 FeO cotectic line is tightly constrained. Figure 3a illustrates the liquidus phase relations
165 in the Fe-O-H system. The liquidus field of FeO extends close to the Fe-FeH side, and
166 the ternary peritectic (unlikely eutectic) point should be located at the H-rich portion of
167 the phase diagram. It suggests the presence of the Fe-FeH binary eutectic point at
168 $\text{FeH}_{0.42}$ (Fe + 0.75 wt% H). It includes more hydrogen than the liquid $\text{FeH}_{0.26}$ obtained

169 at 1900 K in run #B, suggesting that the Fe-FeH binary eutectic temperature is
170 somewhat lower than 1900 K at 45 GPa.

171 The Fe-FeH binary eutectic liquid composition may change little with increasing
172 pressure because the high P - T experiments performed by Tagawa, Helffrich et al. (2022)
173 showed that the temperature/pressure slope of the melting curve of stoichiometric FeH
174 is similar to that of Fe at >40 GPa. On the other hand, the present results on the Fe-FeO
175 system as well as earlier experiments (Seagle et al., 2008; Oka et al., 2019) and
176 thermodynamic calculations (Komabayashi, 2014) demonstrate that O concentration in
177 the Fe-FeO binary eutectic liquid increases to 15 wt% with increasing pressure to 330
178 GPa. The Fe-O±C liquids obtained in runs #A5 and #A6 verify the pressure evolution of
179 the Fe-FeO eutectic liquid composition (the composition of liquid that coexists with
180 both Fe and FeO) in the presence of <1 wt% and ~3 wt% C, respectively (Figure S1).
181 By taking the positions of the Fe-FeO and Fe-FeH binary eutectic points into account,
182 we suppose the Fe-O-H ternary liquidus phase relations at the ICB pressure in Figure
183 3b.

184 3.2. Possible Outer Core Liquid Composition

185 Since the outer core crystallizes the dense inner core at the ICB, the liquid composition
186 should be within the liquidus field of Fe at 330 GPa (Figure 3b). It has been
187 demonstrated by earlier experiments on ternary Fe alloy systems containing two light
188 elements—Fe-Si-S (Tateno et al., 2018), Fe-S-O (Yokoo et al., 2019), Fe-Si-C
189 (Hasegawa et al., 2021), and Fe-C-O (Sakai & Hirose, 2021)—that the ternary eutectic
190 point is located close to the tie line between the eutectic points in relevant binary
191 systems; in other words, the liquidus field of Fe (such as a colored area in Figure 3b) in
192 these ternary systems can be approximated by linear interpolation between the eutectic
193 liquid compositions in relevant binary systems. This may be extended to the
194 Fe-O-H-Si-S system that we consider for the liquid outer core; the liquidus field of Fe
195 could be estimated from the four relevant binary eutectic compositions at 330 GPa; Fe
196 with 15 wt% O (Figure S1), 0.75 wt% H (Figure 3b), 8 wt% Si (Hasegawa et al., 2021),
197 or 5 wt% S (Mori et al., 2017).

198 We estimate the possible range of the outer core liquid composition based on three
199 independent constraints (Hirose et al., 2021). First, 1) it must account for the density
200 and P-wave velocity observed in the outer core (Umemoto & Hirose, 2020). We first
201 consider $T_{\text{ICB}} = 5800$ K and 6280 K, which correspond to $T_{360\text{GPa}} = 6000$ K and 6500 K,
202 respectively, when assuming isentropic temperature profiles with Grüneisen parameter γ

203 = 1.5 (Vočadlo et al., 2003); these are the conditions at which the possible inner core
204 composition was examined by Wang et al. (2021). Also, 2) the liquid core composition
205 should be within the liquidus field of Fe in the Fe-O-H-Si±1.7wt%S system at the ICB
206 pressure. Geochemical and cosmochemical estimates have consistently proposed ~2
207 wt% S in the core (Dreibus & Palme, 1996; McDonough, 2014), and here we adopt 0 or
208 1.7 wt% S in the outer core according to Dreibus & Palme. The colored portions in
209 [Figures 4a–d](#) indicate O, H, and Si concentrations in liquids Fe-Ni-O-H-Si±1.7wt%S
210 (Fe/Ni =16 by weight), which meet these two constraints from 1) the outer core density
211 and velocity and 2) the liquidus phase diagram at 330 GPa.

212 In addition, 3) the third constraint is from the possible inner core solid composition that
213 was estimated in Fe-Si-S(-C) by Li et al. (2018) and in Fe-H-Si by Wang et al. (2021),
214 which explains the observed density, P-wave and S-wave velocities (Dziewonski &
215 Anderson, 1981; Kennett et al., 1995). Their calculations of $\text{Fe}_{64-y}\text{Si}_y$ ($y = 0, 4, \text{ and } 8$)
216 and $\text{Fe}_{60}\text{Si}_4\text{H}_z$ ($z = 1, 2, 4, \text{ and } 8$) alloys demonstrated that the density (ρ), P-wave (V_P)
217 and S-wave velocities (V_S) of Fe alloys are written as; $\rho = -0.105y - 0.039z + 13.639(5)$,
218 $V_P = -0.001y - 0.034z + 11.559(128)$, and $V_S = -0.061y - 0.053z + 4.108(154)$ at $T_{360\text{GPa}}$
219 = 6500 K, and $\rho = -0.104y - 0.038z + 13.682(48)$, $V_P = 0.001y - 0.019z + 11.619(110)$,
220 and $V_S = -0.060y - 0.033z + 4.229(140)$ at $T_{360\text{GPa}} = 6000$ K. The inner core may include
221 1.4 wt% S, which is calculated from the 1.7 wt% S in the outer core and the solid/liquid
222 partition coefficient of S, $D_S = 0.8$ by weight at 330 GPa (Alfè et al., 2002; Yokoo et al.,
223 2019). Since Wang et al. (2021) mentioned that the effects of S and Si on the density
224 and sound velocities are similar to each other, we consider that the effect of S is
225 equivalent to that of Si. O is not partitioned into solid Fe and thus not considered in the
226 inner core (Alfè et al., 2002; Ozawa et al., 2010). With these relations, we obtain the
227 possible ranges of the inner core composition in the Fe-H-Si±1.4wt%S system,
228 depending on temperature. It gives the liquid outer core composition based on the
229 solid/liquid partition coefficients $D_H = 0.89$ (from run #A-4 in this study) and $D_{\text{Si}} = 1.0$
230 by weight (Alfè et al., 2002; Kuwayama & Hirose, 2004). The $D_H = 0.77\text{--}0.89$ obtained
231 in this study at 39–45 GPa is slightly higher than 0.72–0.74 reported by earlier
232 multi-anvil experiments at 15–20 GPa (Imai, 2013). The compositional ranges of liquids
233 in chemical equilibrium with the possible inner core solid are illustrated by areas
234 enclosed by black lines in [Figures 4a–d](#).

235 The overlap between the colored area (constrained by the outer core density and
236 velocity and by the liquidus field of Fe) and the black enclosed area (constrained by the
237 inner core density and velocities) in [Figures 4a–d](#) indicates the possible compositional

238 range for the liquid outer core. It becomes smaller with 1.7 and 1.4 wt% S respectively
239 in the outer and inner core than in S-free cases. Possible liquid compositions are not
240 found in the Fe-O-H-Si-1.7wt%S system when $T_{\text{ICB}} = 5800$ K ($T_{360\text{GPa}} = 6000$ K)
241 (Figure 4c). If $T_{\text{ICB}} = 6280$ K ($T_{360\text{GPa}} = 6500$ K), the outer core may include 2.9–5.2
242 wt% O, 0.03–0.32 wt% H, and 0–3.4 wt% Si and in addition to 1.7 wt% S. Furthermore,
243 with T_{ICB} of ~ 6000 K, the H-rich liquid core with ~ 0.3 wt% H and ~ 3 wt% O in addition
244 to 1.7 wt% S and minimal Si satisfies the seismological and liquidus-phase constraints
245 considered here (Figures 4c, d). It suggests that ~ 1 wt% H_2O in the bulk Earth,
246 corresponding to about 50 ocean mass of water, is sequestered in the core (Tagawa et
247 al., 2021; Li et al., 2020; Yuan & Steinle-Neumann, 2020). It is supported by recent
248 planet formation theories that a large amount of water was brought to the Earth during
249 its accretion (Raymond et al., 2007; Walsh et al., 2011). The range of the O content is
250 still consistent with the recent estimate of <3.8 wt% O in the outer core to explain the
251 density jump across the ICB, which was based on the experimentally-determined
252 equations of state of liquid and solid Fe (Kuwayama et al., 2020; Dewaele et al., 2006).
253 Indeed, ~ 0.2 wt.% C could be also present in the core (Fischer et al., 2020), but it hardly
254 decreases the present estimates of the core inventories of other light elements.

255 The $T_{\text{ICB}} = 6000$ – 6280 K, however, corresponds to about 4400 – 4600 K at the CMB
256 when $\gamma = 1.5$ (Vočadlo et al., 2003). It is much higher than the solidus temperatures of
257 the pyrolitic and chondritic mantle materials at 135 GPa (Fiquet et al., 2010; Andrault et
258 al., 2011; Nomura et al., 2014; Kim et al., 2020). It could therefore lead to extensive
259 melting in the lowermost mantle at present, but seismology reveals the presence of
260 partial melts only locally at ultralow velocity zones above the CMB. It is necessary to
261 better constrain the core temperature to further explore the possible core composition
262 (Hirose et al., 2021).

263 4. Conclusions

264 We obtained the liquidus phase relations in the Fe-O-H ternary and Fe-H binary systems
265 at ~ 40 GPa. While earlier studies reported that Fe and stoichiometric FeH form
266 continuous solid solution below ~ 20 GPa (Sakamaki et al., 2009; Imai, 2013; Shibazaki
267 et al., 2014), our results at ~ 40 GPa indicate eutectic melting between Fe and FeH from
268 the observations that 1) $\text{FeH}_{0.20}$ was formed with the hcp structure, different from fcc for
269 stoichiometric FeH, suggesting a miscibility gap between the H-poor hcp and H-rich fcc
270 phases in Fe-FeH, 2) the liquidus temperature of $\text{FeH}_{0.26}$ is 1900 K, lower than the
271 melting temperature of FeH (Tagawa, Helffrich et al., 2022), and 3) melting phase

272 relations in the Fe-O-H ternary require the eutectic point in the Fe-FeH system. The
273 Fe-FeH eutectic liquid composition is found to be FeH_{0.42} (Fe + 0.75 wt% H) at this
274 pressure. The pressure effect on the Fe-FeH eutectic liquid composition is likely to be
275 small because the temperature/pressure slope of the melting curve of FeH is comparable
276 to that of Fe (Tagawa, Helffrich et al., 2022). On the other hand, the present study
277 combined with earlier experiments demonstrates that O concentration in the Fe-FeO
278 binary eutectic liquid increases to 15 wt% at 330 GPa. These allow us to extrapolate the
279 liquidus phase relations in the Fe-O-H system to 330 GPa.

280 We estimated the possible range of the outer core liquid composition to be Fe + 2.9–5.2
281 wt% O + 0.03–0.32 wt% H + 0–3.4 wt% Si + 1.7 wt% S when $T_{\text{ICB}} = 6280$ K, based on
282 constraints from 1) the liquidus field of Fe (in order to crystallize the dense inner core),
283 2) the outer core density and velocity, and 3) the inner core density and velocities (the
284 outer core composition is calculated from that of the inner core using the solid-liquid
285 partition coefficients of light elements at ICB conditions). If T_{ICB} is ~6000 K, the outer
286 core is enriched in both O and H, supporting recent arguments on the delivery of a large
287 amount of water to the growing Earth and its incorporation into core metals for the most
288 part.

289 **Data Availability Statement**

290 Datasets for this research are found in [Tables S1](#), [S2](#), and [Dataset S1](#) available online
291 (from <https://doi.org/10.5281/zenodo.6508681>).

292 **Acknowledgments**

293 We thank K. Yonemitsu for sample analyses with FIB, EDS, and FE-EPMA. Comments
294 from anonymous reviewers were helpful to improve the manuscript. This work was
295 supported by the JSPS research grants 16H06285 and 21H04968 to K.H. XRD
296 measurements were performed at BL10XU, SPring-8 (proposals no. 2019A0072,
297 2019B0072, and 2021B0181).

298 **References**

299 Alfè, D., Gillan, M. J., & Price, G. D. (2002). Composition and temperature of the
300 earth's core constrained by combining ab initio calculations and seismic data. *Earth*
301 *and Planetary Science Letters*, 195, 91–98.
302 [https://doi.org/10.1016/S0012-821X\(01\)00568-4](https://doi.org/10.1016/S0012-821X(01)00568-4)

303 Andraut, D., Bolfan-Casanova, N., Nigro, G. Lo, Bouhifd, M. A., Garbarino, G., &
304 Mezouar, M. (2011). Solidus and liquidus profiles of chondritic mantle: implication
305 for melting of the Earth across its history. *Earth and Planetary Science Letters*, *304*,
306 251–259. <https://doi.org/10.1016/j.epsl.2011.02.006>

307 Badro, J., Cote, A. S., & Brodholt, J. P. (2014). A seismologically consistent
308 compositional model of Earth’s core. *Proceedings of the National Academy of*
309 *Science of the United States of America*, *111*, 7542–7545.
310 <https://doi.org/10.1073/pnas.1316708111>

311 Dreibus, G., & Palme, H. (1996). Cosmochemical constraints on the sulfur content in
312 the Earth’s core. *Geochimica et Cosmochimica Acta*, *60*, 1125–1130.
313 [https://doi.org/10.1016/0016-7037\(96\)00028-2](https://doi.org/10.1016/0016-7037(96)00028-2)

314 Dziewonski, A. M., & Anderson, D. L. (1981). Preliminary reference Earth model.
315 *Physics of the Earth and Planetary Interiors*, *25*, 297–356.
316 [https://doi.org/10.1016/0031-9201\(81\)90046-7](https://doi.org/10.1016/0031-9201(81)90046-7)

317 Fukai, Y. (1992). Some properties of the Fe-H system at high pressures and
318 temperatures, and their implications for the Earth’s core. In Y. Syono, M.H.
319 Manghnani (Eds.), *High-pressure research: applications to Earth and planetary*
320 *sciences* (Vol. 67, pp. 373–385). <https://doi.org/10.1029/GM067p0373>

321 Fischer, R. A., Cottrell, E., Hauri, E., Lee, K. K. M., & Le Voyer, M. (2020). The carbon
322 content of Earth and its core. *Proceedings of the National Academy of Sciences of the*
323 *United States of America*, *117*, 8743–8749.
324 <https://doi.org/10.1073/pnas.1919930117>

325 Fiquet, G., Auzende, A. L., Siebert, J., Corgne, A., Bureau, H., Ozawa, H., & Garbarino,
326 G. (2010). Melting of peridotite to 140 gigapascals. *Science*, *329*, 1516–1518.
327 <https://doi.org/10.1126/science.1192448>

328 Hasegawa, M., Hirose, K., Oka, K., & Ohishi, Y. (2021). Liquidus phase relations and
329 solid-liquid partitioning in the Fe-Si-C system under core pressures. *Geophysical*
330 *Research Letters*, *48*, e2021GL092681. <https://doi.org/10.1029/2021GL092681>

331 Hirose, K., Wood, B., & Vočadlo, L. (2021). Light elements in the Earth’s core. *Nature*
332 *Reviews Earth & Environment*, *2*, 645–658.
333 <https://doi.org/10.1038/s43017-021-00203-6>

334 Ikoma, M., & Genda, H. (2006). Constraints on the mass of a habitable planet with
335 water of nebular origin. *The Astrophysical Journal*, *648*, 696.
336 <https://doi.org/10.1086/505780>

337 Imai, T. (2013). *Crystal/melt partitioning under deep mantle conditions and melting*
338 *phase relation in the system Fe-FeH* (PhD thesis). Tokyo Institute of Technology

339 Kato, C., Umemoto, K., Ohta, K., Tagawa, S., Hirose, K., & Ohishi, Y. (2020). Stability
340 of fcc phase FeH to 137 GPa. *American Mineralogist*, *105*, 917–921.
341 <https://doi.org/10.2138/am-2020-7153>

342 Kennett, B. L. N., Engdahl, E. R., & Buland, R. (1995). Constraints on seismic
343 velocities in the Earth from traveltimes. *Geophysical Journal International*, *122*,
344 108–124. <https://doi.org/10.1111/j.1365-246X.1995.tb03540.x>

345 Kim, T., Ko, B., Greenberg, E., Prakapenka, V., Shim, S. H., & Lee, Y. (2020). Low
346 melting temperature of anhydrous mantle materials at the core-mantle boundary.
347 *Geophysical Research Letters*, *47*, 1–10. <https://doi.org/10.1029/2020GL089345>

348 Komabayashi, T. (2014). Thermodynamics of melting relations in the system Fe-FeO at
349 high pressure: implications for oxygen in the Earth's core. *Journal of Geophysical
350 Research: Solid Earth*, *119*, 4164–4177. <https://doi.org/10.1002/2014JB010980>

351 Komabayashi, T., Fei, Y., Meng, Y., & Prakapenka, V. (2009). In-situ X-ray diffraction
352 measurements of the γ - ϵ transition boundary of iron in an internally-heated diamond
353 anvil cell. *Earth and Planetary Science Letters*, *282*, 252–257.
354 <https://doi.org/10.1016/j.epsl.2009.03.025>

355 Kuwayama, Y., & Hirose, K. (2004). Phase relations in the system Fe-FeSi at 21 GPa.
356 *American Mineralogist*, *89*, 273–276. <https://doi.org/10.2138/am-2004-2-303>

357 Kuwayama, Y., Morard, G., Nakajima, Y., Hirose, K., Baron, A. Q. R., Kawaguchi, S. I.,
358 et al. (2020). Equation of state of liquid iron under extreme conditions. *Physical
359 Review Letters*, *124*, 165701. <https://doi.org/10.1103/PhysRevLett.124.165701>

360 Li, J., & Fei, Y. (2014). Experimental constraints on core composition. In *Treatise on
361 geochemistry* (2nd ed., Vol. 3, pp. 527–557). Amsterdam. Elsevier.
362 <https://doi.org/10.1016/b978-0-08-095975-7.00214-x>

363 Li, Y., Vočadlo, L., Brodholt, J. P. (2018). The elastic properties of hcp-Fe alloys
364 under the conditions of the Earth's inner core. *Earth and Planetary Science Letters*,
365 *493*, 118–127. <https://doi.org/10.1016/j.epsl.2018.04.013>

366 Li, Y., Vočadlo, L., Sun, T., & Brodholt, J. P. (2020). The Earth's core as a reservoir of
367 water. *Nature Geoscience*, *13*, 453–458. <https://doi.org/10.1038/s41561-020-0578-1>

368 McDonough, W. F. (2014). Compositional model for the Earth's core. In *Treatise on
369 geochemistry* (2nd ed., Vol. 3, pp. 559–577). Amsterdam. Elsevier.
370 <https://doi.org/10.1016/B978-0-08-095975-7.00215-1>

371 Morard, G., Andraut, D., Antonangeli, D., Nakajima, Y., Auzende, A. L., Boulard, E., et
372 al. (2017). Fe-FeO and Fe-Fe₃C melting relations at Earth's core-mantle boundary
373 conditions: implications for a volatile-rich or oxygen-rich core. *Earth and Planetary
374 Science Letters*, *473*, 94–103. <https://doi.org/10.1016/j.epsl.2017.05.024>

375 Mori, Y., Ozawa, H., Hirose, K., Sinmyo, R., Tateno, S., Morard, G., & Ohishi, Y.
376 (2017). Melting experiments on Fe–Fe₃S system to 254 GPa. *Earth and Planetary*
377 *Science Letters*, 464, 135–141. <https://doi.org/10.1016/j.epsl.2017.02.021>

378 Nomura, R., Hirose, K., Uesugi, K., Ohishi, Y., Tsuchiyama, A., Miyake, A., & Ueno, Y.
379 (2014). Low core-mantle boundary temperature inferred from the solidus of pyrolite.
380 *Science*, 343, 522–525. <https://doi.org/10.1126/science.1248186>

381 Oka, K., Hirose, K., Tagawa, S., Kidokoro, Y., Nakajima, Y., Kuwayama, Y., et al.
382 (2019). Melting in the Fe-FeO system to 204 GPa: implications for oxygen in Earth's
383 core. *American Mineralogist*, 104, 1603–1607.
384 <https://doi.org/10.2138/am-2019-7081>

385 Olson, P. L., & Sharp, Z.D. (2019). Nebular atmosphere to magma ocean: a model for
386 volatile capture during Earth accretion. *Physics of the Earth and Planetary Interiors*,
387 294, 106294. <https://doi.org/10.1016/j.pepi.2019.106294>

388 Ozawa, H., Hirose, K., Tateno, S., Sata, N., & Ohishi, Y. (2010). Phase transition
389 boundary between B1 and B8 structures of FeO up to 210GPa. *Physics of the Earth*
390 *and Planetary Interiors*, 179, 157–163. <https://doi.org/10.1016/j.pepi.2009.11.005>

391 Raymond, S. N., Quinn, T., & Lunine, J. I. (2007). High-resolution simulations of the
392 final assembly of Earth-like planets. 2. Water delivery and planetary habitability.
393 *Astrobiology*, 7, 66–84. <https://doi.org/10.1089/ast.2006.06-0126>.

394 Sakai, F., & Hirose, K. (2021). Melting experiments on the Fe-C-O ternary system
395 under core pressures. JpGU Meeting Abstract

396 Sakamaki, K., Takahashi, E., Nakajima, Y., Nishihara, Y., Funakoshi, K., Suzuki, T., &
397 Fukai, Y. (2009). Melting phase relation of FeH_x up to 20 GPa: implication for the
398 temperature of the Earth's core. *Physics of the Earth and Planetary Interiors*, 174,
399 192–201. <https://doi.org/10.1016/j.pepi.2008.05.017>

400 Seagle, C. T., Heinz, D. L., Campbell, A. J., Prakapenka, V. B., & Wanless, S. T. (2008).
401 Melting and thermal expansion in the Fe-FeO system at high pressure. *Earth and*
402 *Planetary Science Letters*, 265, 655–665. <https://doi.org/10.1016/j.epsl.2007.11.004>

403 Scheler, T., Degtyareva, O., & Gregoryanz, E. (2011). On the effects of high
404 temperature and high pressure on the hydrogen solubility in rhenium. *Journal of*
405 *Chemical Physics*, 135, 214501. <https://doi.org/10.1063/1.3652863>

406 Shibazaki, Y., Terasaki, H., Ohtani, E., Tateyama, R., Nishida, K., Funakoshi, K., &
407 Higo, Y. (2014). High-pressure and high-temperature phase diagram for Fe_{0.9}Ni_{0.1}-H
408 alloy. *Physics of the Earth and Planetary Interiors*, 228, 192–201.
409 <https://doi.org/10.1016/j.pepi.2013.12.013>

410 Stixrude, L. (2012). Structure of iron to 1 Gbar and 40 000 K. *Physical Review Letters*,
411 108, 055505. <https://doi.org/10.1103/PhysRevLett.108.055505>

412 Tagawa, S., Sakamoto, N., Hirose, K., Yokoo, S., Hernlund, J., Ohishi, Y., & Yurimoto,
413 H. (2021). Experimental evidence for hydrogen incorporation into Earth's core.
414 *Nature Communications*, 12, 2588. <https://doi.org/10.1038/s41467-021-22035-0>

415 Tagawa, S., Gomi, H., Hirose, K., & Ohishi, Y. (2022). High-temperature equation of
416 state of FeH: implications for hydrogen in Earth's inner core. *Geophysical Research*
417 *Letters*, 49, e2021GL096260. <https://doi.org/10.1029/2021GL096260>

418 Tagawa, S., Helffrich, G., Hirose, K., Ohishi, Y. (2022). High-Pressure melting curve of
419 FeH: implications for eutectic melting between Fe and non-magnetic FeH. *Earth and*
420 *Space Science Open Archive*.
421 <https://www.essoar.org/doi/abs/10.1002/essoar.10510818.1>

422 Tateno, S., Hirose, K., Sinmyo, R., Morard, G., Hirao, N., & Ohishi, Y. (2018). Melting
423 experiments on Fe–Si–S alloys to core pressures: silicon in the core? *American*
424 *Mineralogist*, 103, 742–748. <https://doi.org/10.2138/am-2018-6299>

425 Thompson, E. C., Davis, A. H., Bi, W., Zhao, J., Alp, E. E., Zhang, D., et al. (2018).
426 High-pressure geophysical properties of fcc phase FeH_x. *Geochemistry, Geophysics,*
427 *Geosystems*, 19, 305–314. <https://doi.org/10.1002/2017GC007168>

428 Umemoto, K., & Hirose, K. (2015). Liquid iron-hydrogen alloys at outer core
429 conditions by first-principles calculations. *Geophysical Research Letters*, 42, 7513–
430 7520. <https://doi.org/10.1002/2015GL065899>

431 Umemoto, K., & Hirose, K. (2020). Chemical compositions of the outer core examined
432 by first principles calculations. *Earth and Planetary Science Letters*, 531, 116009.
433 <https://doi.org/10.1016/j.epsl.2019.116009>

434 Vočadlo, L., Alfè, D., Gillan, M. J., & Price, G. D. (2003). The properties of iron under
435 core conditions from first principles calculations. *Physics of the Earth and Planetary*
436 *Interiors*, 140, 101–125. <https://doi.org/10.1016/j.pepi.2003.08.001>

437 Walsh, K. J., Morbidelli, A., Raymond, S. N., O'brien, D. P., & Mandell, A. M. (2011).
438 A low mass for Mars from Jupiter's early gas-driven migration. *Nature*, 475, 206–
439 209. <https://doi.org/10.1038/nature10201>

440 Wang, W., Li, Y., Brodholt, J. P., Vočadlo, L., Walter, M. J., & Wu, Z. (2021). Strong
441 shear softening induced by superionic hydrogen in Earth's inner core. *Earth and*
442 *Planetary Science Letters*, 568, 117014. <https://doi.org/10.1016/j.epsl.2021.117014>

443 Yokoo, S., Hirose, K., Sinmyo, R., & Tagawa, S. (2019). Melting experiments on
444 liquidus phase relations in the Fe-S-O ternary system under core pressures.

445 *Geophysical Research Letters*, 46, 5137–5145.
446 <https://doi.org/10.1029/2019GL082277>
447 Yuan, L., & Steinle-Neumann, G. (2020). Strong sequestration of hydrogen into the
448 Earth's core during planetary differentiation. *Geophysical Research Letters*, 47,
449 e2020GL088303. <https://doi.org/10.1029/2020GL088303>

450 **References From the Supporting Information**

451 Akahama, Y., & Kawamura, H. (2004). High-pressure Raman spectroscopy of diamond
452 anvils to 250 GPa: method for pressure determination in the multimegabar pressure
453 range. *Journal of Applied Physics*, 96, 3748–3751. <https://doi.org/10.1063/1.1778482>
454 Badro, J., Siebert, J., & Nimmo, F. (2016). An early geodynamo driven by exsolution of
455 mantle components from Earth's core. *Nature*, 536, 326–328.
456 <https://doi.org/10.1038/nature18594>
457 Caracas, R. (2015). The influence of hydrogen on the seismic properties of solid iron.
458 *Geophysical Research Letters*, 42, 3780–3785.
459 <https://doi.org/10.1002/2015GL063478>
460 Chi, Z., Nguyen, H., Matsuoka, T., Kagayama, T., Hirao, N., Ohishi, Y., & Shimizu, K.
461 (2011). Cryogenic implementation of charging diamond anvil cells with H₂ and D₂.
462 *Review of Scientific Instruments*, 82, 105109. <https://doi.org/10.1063/1.3652981>
463 Dewaele, A., & Torrent, M. (2013). Equation of state of α -Al₂O₃. *Physical Review B*, 88,
464 064107. <https://doi.org/10.1103/PhysicalReviewB.88.064107>
465 Dewaele, A. S., Loubeyre, P., Occelli, F., Mezouar, M., Dorogokupets, P. I., & Torrent,
466 M. (2006). Quasihydrostatic equation of state of iron above 2 Mbar. *Physical Review*
467 *Letters*, 97, 215504. <https://doi.org/10.1103/PhysicalReviewLetters.97.215504>
468 Dorogokupets, P. I., Dymshits, A. M., Litasov, K. D., & Sokolova, T. S. (2017).
469 Thermodynamics and equations of state of iron to 350 GPa and 6000 K. *Scientific*
470 *Reports*, 7, 41863. <https://doi.org/10.1038/srep41863>
471 Helffrich, G. (2014). Outer core compositional layering and constraints on core liquid
472 transport properties. *Earth and Planetary Science Letters*, 391, 256–262.
473 <https://doi.org/10.1016/j.epsl.2014.01.039>
474 Helffrich, G., Hirose, K., & Nomura, R. (2020). Thermodynamical modeling of liquid
475 Fe-Si-Mg-O: molten magnesium silicate release from the core. *Geophysical*
476 *Research Letters*, 47, e2020GL089218. <https://doi.org/10.1029/2020GL089218>
477 Hirao, N., Kawaguchi, S. I., Hirose, K., Shimizu, K., Ohtani, E., & Ohishi, Y. (2020).
478 New developments in high-pressure X-ray diffraction beamline for diamond anvil

479 cell at SPring-8. *Matter and Radiation at Extremes*, 5, 018403.
480 <https://doi.org/10.1063/1.5126038>

481 Hirose, K., Tagawa, S., Kuwayama, Y., Sinmyo, R., Morard, G., Ohishi, Y., & Genda, H.
482 (2019). Hydrogen limits carbon in liquid iron. *Geophysical Research Letters*, 46,
483 5190–5197. <https://doi.org/10.1029/2019GL082591>

484 Iizuka-Oku, R., Yagi, T., Gotou, H., Okuchi, T., Hattori, T., & Sano-Furukawa, A.
485 (2017). Hydrogenation of iron in the early stage of Earth’s evolution. *Nature*
486 *Communications*, 8, 14096. <https://doi.org/10.1038/ncomms14096>

487 Ikuta, D., Ohtani, E., Sano-Furukawa, A., Shibazaki, Y., Terasaki, H., Yuan, L., &
488 Hattori, T. (2019). Interstitial hydrogen atoms in face-centered cubic iron in the
489 Earth’s core. *Scientific Reports*, 9, 7108. <https://doi.org/10.1038/s41598-019-43601-z>

490 Ohta, K., Ichimaru, K., Einaga, M., Kawaguchi, S., Shimizu, K., Matsuoka, T., et al.
491 (2015). Phase boundary of hot dense fluid hydrogen. *Scientific Reports*, 5, 16560.
492 <https://doi.org/10.1038/srep16560>

493 Seto, Y., Nishio-Hamane, D., Nagai, T., & Sata, N. (2010). Development of a software
494 suite on X-ray diffraction experiments. *The Review of High Pressure Science and*
495 *Technology*, 20, 269–276

496

497 **Figure 1.** XRD patterns collected in (a) run #A4 for the Fe-O-H sample and (b) run #B
498 for the Fe-H sample. Hcp, hcp FeH_x; fcc, fcc FeH_x; dhcp, FeH; rB1, rhombohedral B1
499 FeO; cor, corundum (pressure medium); Re, rhenium (gasket). The bottom profile in (b)
500 shows only peaks that appeared upon quenching temperature, which was used to
501 calculate hydrogen concentration in liquid in run #B.

502 **Figure 2.** Sample cross sections and temperature profile in run #A4. Scanning ion
503 microscope image (a) and X-ray map of oxygen (b) show that liquid coexisted with
504 solid Fe and FeO. Crystals were formed from liquid upon quenching temperature, and
505 their unit-cell volumes were used to calculate hydrogen concentration in liquid.
506 Temperature at the liquid/solid boundary is obtained by a combination of these images
507 and a temperature profile (c).

508 **Figure 3.** Liquidus phase diagrams of the Fe-FeO-FeH ternary system. Green lines are
509 cotectic lines that separate the liquidus fields of Fe, FeO, and FeH. In (a) for ~40 GPa,
510 diamond, circles, and square show the compositions of liquids coexisting with Fe, FeO
511 and Fe + FeO, respectively (filled and open circle/square symbols indicate 0.1–0.4 wt%
512 and 1.7 wt% C in liquids, respectively). The Fe-FeO eutectic liquid composition is
513 given by a red triangle from [Figure S1](#). The Fe-FeH eutectic liquid composition may be
514 FeH_{0.42} (Fe + 0.75 wt% H). (b) The liquidus phase relations extrapolated to 330 GPa
515 considering the Fe-FeO (orange triangle, [Figure S1](#)) and Fe-FeH binary eutectic liquid
516 compositions (the latter could exhibit little pressure dependence). The liquidus field of
517 Fe at ICB conditions is illustrated by a blue area.

518 **Figure 4.** Possible ranges of the outer core liquid composition in the
519 Fe-O-Si-H±1.7wt%S system. Colored areas show liquid compositions that are
520 compatible with the observed outer core density and P-wave velocity (Umemoto &
521 Hirose, 2020) and within the liquidus field of Fe. The areas enclosed by black lines
522 indicate liquid compositions that are in equilibrium with the possible compositions of
523 the inner core solid that explain observed density, P- and S-wave velocities (Li et al.,
524 2018; Wang et al., 2021). If T_{CMB} is ~6000 K, the outer core may include ~3 wt% O and
525 ~0.3 wt% H as important light elements.

Figure 1.

Figure 2.

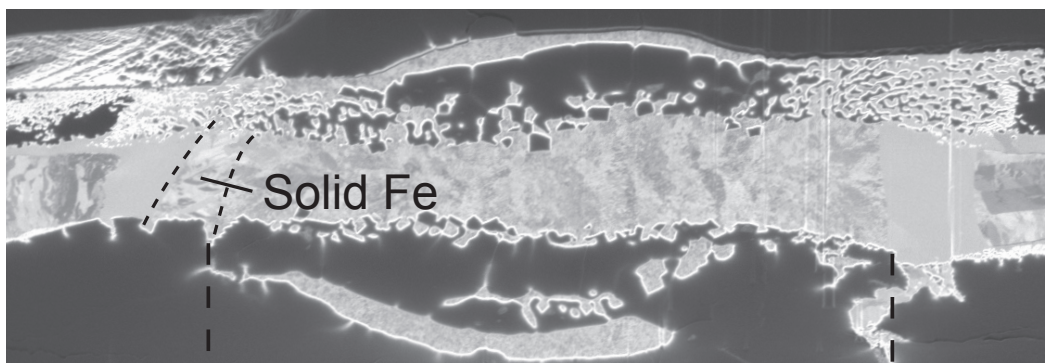
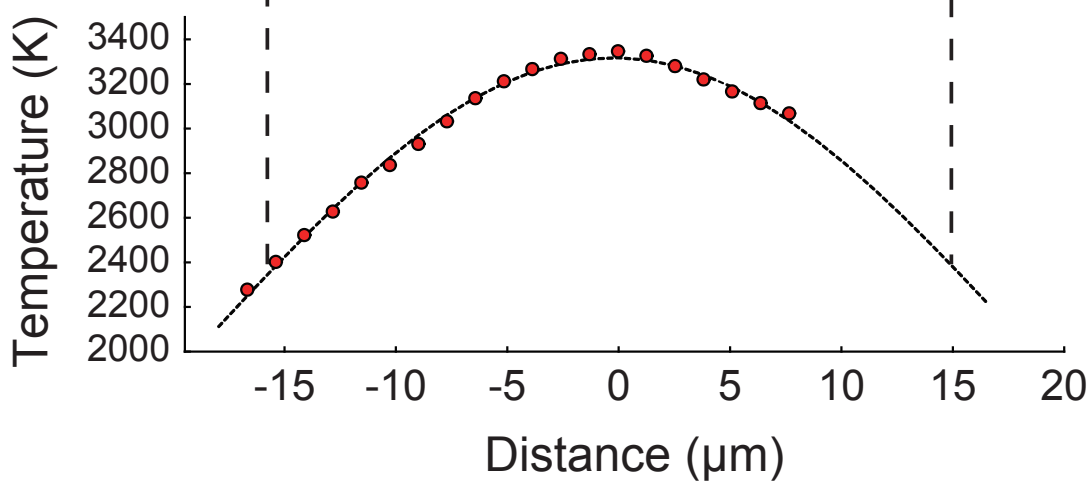
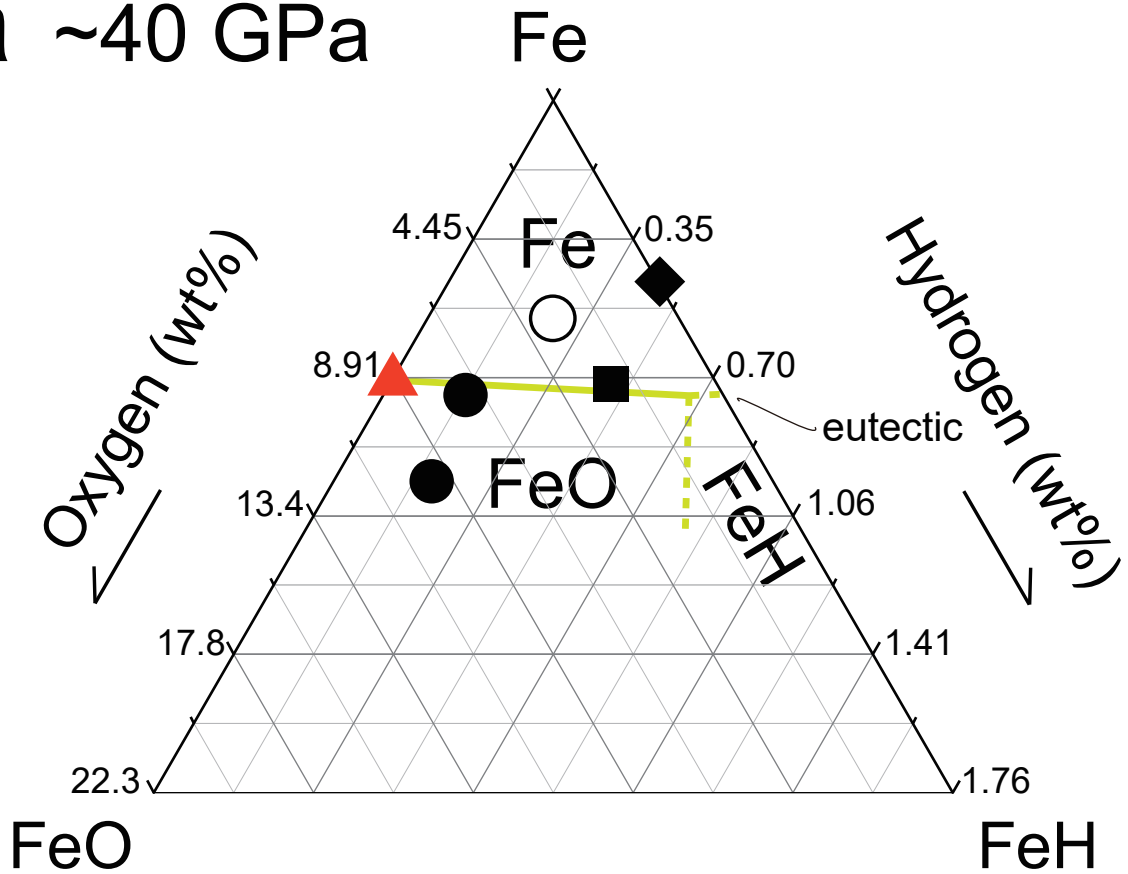
a10 μ m**b****c**

Figure 3.

a ~40 GPa



b ~330 GPa

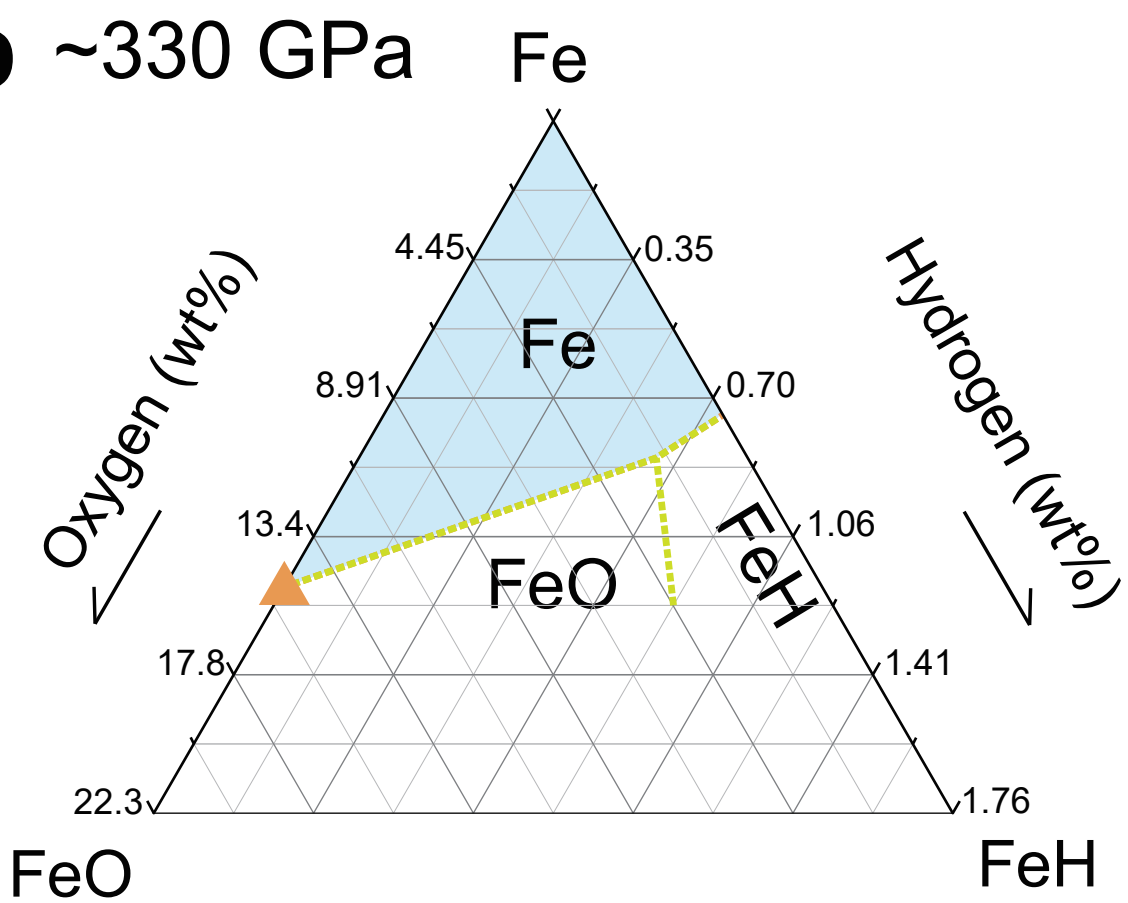


Figure 4.

